

Think about boundary: Fusing multi-level boundary information for landmark heatmap regression

Jinheng Xie Jun Wan Linlin Shen Zhihui Lai

Computer Vision Institute, School of Computer Science & Software Engineering, Shenzhen University

sierkinhane@163.com, junwan2014@whu.edu.cn, llshen@szu.edu.com, lai_zhi_hui@163.com

Abstract

Although current face alignment algorithms have obtained pretty good performances at predicting the location of facial landmarks, huge challenges remain for faces with severe occlusion and large pose variations, etc. On the contrary, semantic location of facial boundary is more likely to be reserved and estimated on these scenes. Therefore, we study a two-stage but end-to-end approach for exploring the relationship between the facial boundary and landmarks to get boundary-aware landmark predictions, which consists of two modules: the self-calibrated boundary estimation (SCBE) module and the boundary-aware landmark transform (BALT) module. In the SCBE module, we modify the stem layers and employ intermediate supervision to help generate high-quality facial boundary heatmaps. Boundary-aware features inherited from the SCBE module are integrated into the BALT module in a multi-scale fusion framework to better model the transformation from boundary to landmark heatmap. Experimental results conducted on the challenging benchmark datasets demonstrate that our approach outperforms state-of-the-art methods in the literature. The code and models will be available at <https://github.com/CVI-SZU/TAB>

1. Introduction

The task of face alignment, i.e. facial landmark localization, is to detect a pre-defined keypoints of 2D face images, which is an essential pre-processing procedure for many face applications such as face recognition [42] [11], face reconstruction [49] [17], facial expression analysis and face edition. Generally, there is a semantic geometric structure meaning of facial landmarks, such as cheek, lips, and eyebrows, etc., as shown in Fig. 2. These geometric structure information of faces is more likely to be reserved and estimated on unconstrained and complicated scenes, such as faces with occlusion, large pose, and make-up, etc.

The definition of the facial boundary is proposed by Wu,

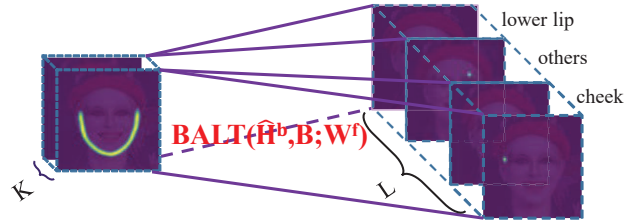


Figure 1. Boundary-aware landmark transform. The location of facial landmarks rely on the facial boundary, it is apparently that the landmark heatmaps can be obtained by transforming these facial boundary heatmaps. Therefore, the BALT module was proposed to estimate this mapping relationship to enhance the shape constraint of facial boundary on facial landmarks.

et al. [53], they design a two-stage method to regress the coordinates of facial landmarks. The approach proposes a boundary heatmap estimator for extracting the boundary information of faces and a boundary-aware landmark regressor for regressing the coordinates of facial landmarks. However, we argue that using input heatmap fusion to highlight the boundary area of image and feature map fusion to directly regress the coordinates of facial landmarks does not make full use of the facial boundary information. There are four reasons for this claim: (1) In the landmark regressor, using input image fusion to highlight facial boundary will increase the channels of input, which significantly increase the computation and complexity of shallow convolutional layers. And the rich boundary-aware features extracted by the boundary estimator are not fully explored. (2) They use a network to directly regress the coordinates of faces, which did not take into account the advantage of the spatial constraints between facial landmarks. To learn a transformation between boundary and landmark heatmaps(matrix-matrix mapping) to get the final landmark predictions seems more reasonable (illustrated by Fig. 1). (3) At the end of the landmark regressor, the downsampled heatmaps will impair the shape constraint on facial landmark predictions, due to the lost boundary information. To make full use of the rich

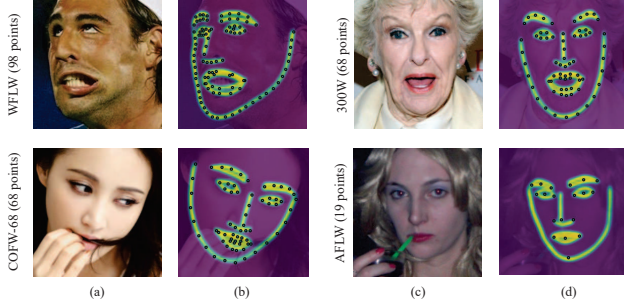


Figure 2. Examples of facial landmark annotations and facial boundaries across different datasets. The WFLW, COFW-68, 300W, and AFLW datasets were labeled with 98 landmarks, 68 landmarks, 68 landmarks, and 19 landmarks, respectively. For all datasets, we use 15 boundaries to represent their boundary information.

facial boundary information, we investigate a two-stage but end-to-end method for exploring the relationship between facial boundary and landmarks to get boundary-aware landmark heatmap predictions, in which boundary-aware features can be used to accelerate the convergence of training and enhance the shape constraint of facial boundary on facial landmark heatmap predictions.

Our approach mainly consists of two modules, the self-calibrated boundary estimation (SCBE) and the boundary-aware landmark transform (BALT). Based on the Stacked Hourglass Network [35], SCBE is mainly used to estimate the boundary information of faces. To improve the performance of SCBE module on faces with severe occlusion and large pose, etc., we replace the stem layers of original Stacked Hourglass Network with VGG [43]/ResNet [22], and initialize them with parameters pre-trained on ImageNet [10] to accelerate the convergence of training. Moreover, SCBE module can self-calibrate the boundary heatmap predictions by introducing intermediate supervision. The BALT module is an Encode-Decode Network based on UNet [39], which can inherit the multi-level boundary information from SCBE module to obtain more accurate landmark heatmaps in a transformation manner. Compared to mapping heatmaps to coordinates, we believe that neural network is more easily to learn the mapping between boundary heatmaps and landmark heatmaps, due to their same spatial representation. In addition, we integrate a multi-scale feature fusion module into the encoding process to fully use the boundary-aware features extracted by the SCBE module. A multi-level shape constraint enhancement is also proposed to enhance the shape constraint of facial boundary on landmarks to get boundary-aware landmark heatmap predictions. Finally, the mean squared error is adopted to combine the two modules to obtain an end-to-end process. The main contributions of this paper can be



Figure 3. Facial boundary heatmaps. 15 boundaries are used to represent the boundary of the face, and the 16th heatmap is a union of all boundaries.

summarized as below:

- We study the effect of stem layers and intermediate supervision for facial boundary estimation to improve the SCBE module’s robustness on unconstrained faces and boost the performance of the BALT module.
- Instead of directly using boundary heatmaps to regress the coordinates of facial landmarks, we propose to map boundary heatmaps to landmark heatmaps to enhance the efficiency of transformation, due to their same spatial representation.
- We propose multi-scale features fusion to make full use of the boundary-aware features extracted by the SCBE module, which accelerate the convergence of training and improve the efficiency of transformation from boundary to landmark. We also introduce the multi-level shape constraint enhancement to enhance the shape constraint of facial boundary on landmarks to get boundary-aware heatmap predictions.
- We evaluate our method on the widely used face alignment benchmarks and achieve state-of-the-art performance. Especially on the WFLW dataset, our method achieves significant improvement over state-of-the-art methods.

2. Related works

Active shape model (ASM) [34] and active appearance model (AAM) [8, 41] are milestones of traditional face alignment methods. With rapid development of the Convolutional Neural Networks (CNNs) [29], more and more CNN-based face alignment methods were proposed. These methods generally fall into two categories: numerical regression-based and heatmap regression-based methods.

Numerical regression-based methods leverage the feed-forward framework to get a fast prediction. Its input is a 2D image and output is numerical values. These methods aim to learn a mapping from image to the coordinates of landmarks. Sun et al. [46] use the convolutional neural network for the first time to detect the landmarks of human faces and propose a three-level cascaded convolutional

neural network to obtain the precise position of facial landmarks. Zhang et al. [62] utilize three successive networks to get the coordinates of the bounding box and five facial landmarks. Guo et al. [21] customize an end-to-end network to estimate rotation of head for regularizing landmark localization to predict landmark coordinates, which achieves a fast speed with reasonable performance. Feng et al. [18] design a novel piece-wise loss that can pay more attention on small and medium errors to accelerate the convergence of training and obtain a good performance. Wu et al. [53] propose boundary heatmaps to help the neural network to regress the coordinates of facial landmarks. Wan et al. [51] aim to improve the performance on occluded faces via a face de-occlusion module and a deep regression module. Nevertheless, these methods are generally fast, but not as good as the heatmap regression-based methods.

Heatmap regression-based methods show a better performance than numerical methods. Their final output are heatmaps, which have the same representation with an image in 2D pixels. It is more likely to utilize the spatial location constraint between pixels to learn a mapping from an image to a heatmap. Kowalski et al. [25] design a cascaded network and use the heatmap for face alignment for the first time. Dapogny et al. [9] design a cascaded-UNet to keep the full spatial resolution to regress landmark heatmaps with intermediate supervision. Wang et al. [52] devise a novel loss function to adapt its shape to different types of pixels in the ground truth heatmap, which obtains better regression. Heatmap based methods are also widely used in other vision tasks, such as human pose estimation [6][16][44] and object detection [28], etc.

With extra boundary information. Wu et al. [53] introduce boundary heatmaps to assist landmark coordinates regression. It firstly estimates facial boundary, then input image fusion and features fusion are performed at the beginning of the landmark regressor to regress the coordinates of facial landmarks. While original face image is processed twice in both boundary heatmap and landmark regression, the shape constraint of boundary on landmark is actually weak, due to the downsampling process. The more advanced heatmap regression is not explored as well. Wang et al. [52] simply include the boundary heatmap as the output of network, which plays as a weak supervision to integrate the boundary information. To fully integrate the useful boundary information into the most recent heatmap based landmark regression, we propose a two-stage end-to-end method to explore the relationship between facial boundary and landmark heatmaps. The boundary-aware features learned in the boundary heatmap estimation network are fully explored to enhance the shape constraint of facial boundary on landmark heatmap predictions.

3. Methodology

The proposed method contains two modules: the SCBE module and the BALT module. The SCBE module aims to estimate the facial boundary heatmaps of images. Then, the BALT module takes these boundaries as input and learns a matrix-matrix mapping to transform facial boundary heatmaps to landmark heatmaps with multi-level boundary information fusion. An overview of the proposed method is shown in Fig 4. In the following, we provide more details about each module.

3.1. Self-calibrated boundary estimation module

Wu et al. [53] use an N-Stacked Hourglass Network(N=4 or 8) and a boundary effectiveness discriminator to train a facial boundary estimation model. To simplify the training process and slim the model, we use a 2-Stacked Hourglass Network and emphasize the mutual effect of stem layers and intermediate supervision, which can refine the final boundary heatmap predictions in a self-calibration manner.

As shown in Fig. 3, we use K boundary heatmaps to represent the facial boundary information of an image, which include $K - 1$ facial boundaries such as cheek, lips, and eyebrows, etc., and the K th heatmap, i.e. a union of all boundaries. The SCBE module can be expressed as follows:

$$\hat{\mathbf{H}}^b = SCBE(\mathbf{I}; \mathbf{W}^{s*}, \mathbf{W}^h) \quad (1)$$

Our SCBE module aims to estimate the facial boundary heatmaps $\hat{\mathbf{H}}^b$ from an image \mathbf{I} , \mathbf{W}^{s*} denotes the parameters pre-trained on ImageNet dataset and \mathbf{W}^h denotes the learnable parameters of the N-Stacked Hourglass.

We name the shallow convolutional layers with output from 256×256 to 64×64 as stem layers (illustrated on the left-most of Fig. 4), which can extract more detailed information such as edges and further help to learn more discriminative representations on subsequent convolutional layers. To increase the robustness of stem layers and extract more rich and accurate semantic information, we try to use ResNet and VGG to replace the stem layers of the Hourglass Network designed by [3], and initialize them with parameters \mathbf{W}^{s*} pre-trained on ImageNet dataset. The experimental results shown in Table 8 indicate that, compared with Hourglass and ResNet, VGG achieves lower loss and better performance. See section 4.9 for more details.

While SCBE module only stacks two hourglasses, we also introduce two effective approaches to improve the quality of predicted heatmaps (illustrated by purple solid line on the left-most of Fig. 4): (1) we extract the low-level features from the former layer and reuse it in the next hourglass to enhance the feature representation. (2) we add a boundary heatmap predictions between the two-stacked hourglass to self-calibrate the final boundary heatmap predictions via intermediate supervision.

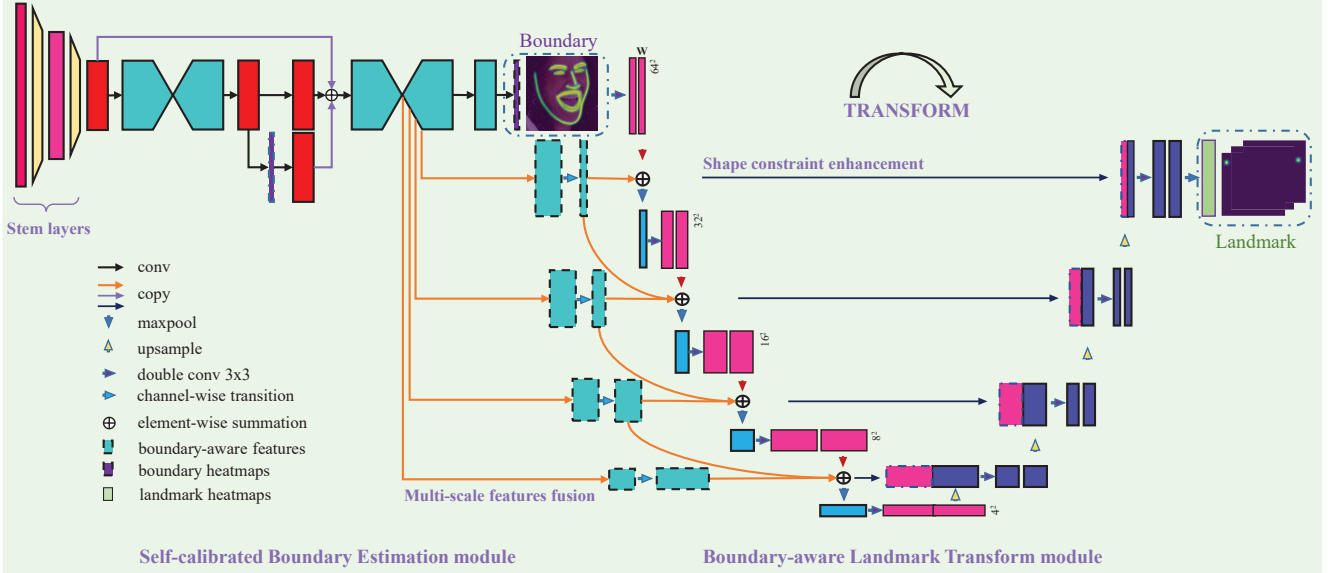


Figure 4. The overall architecture of our model. The SCBE module is used to estimate the facial boundary information of faces. The BALT module is used to learn how to transform the boundary to landmark to get the boundary-sensitive landmark predictions with multi-scale features fusion. The multi-scale features are inherited from the last hourglass of the SCBE module, which encodes a lot of boundary-aware features.

3.2. Boundary-aware landmark transform module

While heatmaps are a set of discrete 2D representations of landmarks, boundary heatmap is a continuous representation of these landmarks and is thus more robust to large pose variations and occlusions. It seems to be more resonable to learn the transformation between the two heatmaps, than the transformation between boundary heatmap and landmark coordinates. The transformation process can be expressed as follows:

$$\hat{\mathbf{H}}^l = \mathcal{BALT}(\hat{\mathbf{H}}^b, \mathbf{B}; \mathbf{W}^f) \quad (2)$$

$\hat{\mathbf{H}}^l$ denotes the predicted facial landmark heatmaps, $\hat{\mathbf{H}}^b$ denotes the predicted facial boundary heatmaps, \mathbf{B} denotes the boundary-aware features extracted by the SCBE module, and \mathbf{W}^f denotes the learnable parameters of the BALT module.

In above section, due to the stem layers and intermediate supervision, our SCBE module obtains refined and accurate boundary heatmaps and learns rich semantic boundary-aware features. To learn a transformation between boundary heatmap and landmark heatmap, we keep the resolution of predicted boundary heatmaps and use it as the input of the BALT module. Then, we fuse the rich and multi-scale boundary-aware features into the encoding and decoding process to enhance the feature representation and the facial boundary constraint on landmark heatmap predictions.

How to choose boundary-aware features? While the feature maps of the last block of SCBE contains high level boundary-aware features, multi-scale features extracted from the last hourglass block (the last light green

block in Fig. 4) could be a good choice to provide more rich information. We visualize the feature maps (64×64) of the last block of SCBE for four example faces (as shown in Fig. 5). One can observe from the figure that they have good perception of boundary in cheek, lips and nose bridge, even when the faces are heavily occluded by hand and masks. We adaptively fuse these multi-level features $\{\mathbf{B}_1, \mathbf{B}_2, \dots, \mathbf{B}_s\}$ and inject them to different levels of the encoder.

How to use these boundary-aware features? Let $\{\mathbf{F}_1^e, \mathbf{F}_2^e, \dots, \mathbf{F}_s^e\}$ represent the outputs of the BALT module in the encoding process, whose resolutions are the same to the s boundary-aware feature maps \mathbf{B} . Each feature map is passed into a channel-transition layer \mathcal{T} , then processed with element-wise summation \oplus , and finally passed into the maxpooling layer \mathcal{MP} and the double convolutional layers \mathcal{DC} :

$$\mathbf{F}_{i+1}^e = \mathcal{DC}(\mathcal{MP}(\mathbf{F}_i^e \oplus \mathcal{T}(\mathbf{B}_i))) \quad (3)$$

It is the $1 \times$ fusion process. For $t \times$ fusion, we add shortcuts between the neighboured convoluntinal layers with different resolutions. The i th fusion process can be formulated as follows::

$$\mathbf{F}_{i+1}^e = \begin{cases} \mathcal{DC}(\mathcal{MP}(\mathbf{F}_i^e \oplus \mathbf{B}'_i)), & (i = 1) \\ \mathcal{DC}(\mathcal{MP}(\mathbf{F}_i^e \oplus \mathbf{B}'_i \oplus \sum_{j=m}^{i-1} \mathbf{B}'_j)), & (i > 1) \end{cases} \quad (4)$$

where \mathbf{B}'_i represents $\mathcal{T}(\mathbf{B}_i)$, \mathbf{B}'_j represents $\mathcal{MP}(\mathcal{T}(\mathbf{B}_j))$, and $m = \text{Max}(1, i - t + 1)$. In the decoding layers, we introduce a shape constraint enhancement module. Let $\{\mathbf{F}_1^d, \mathbf{F}_2^d, \dots, \mathbf{F}_s^d\}$ represent the outputs of the BALT

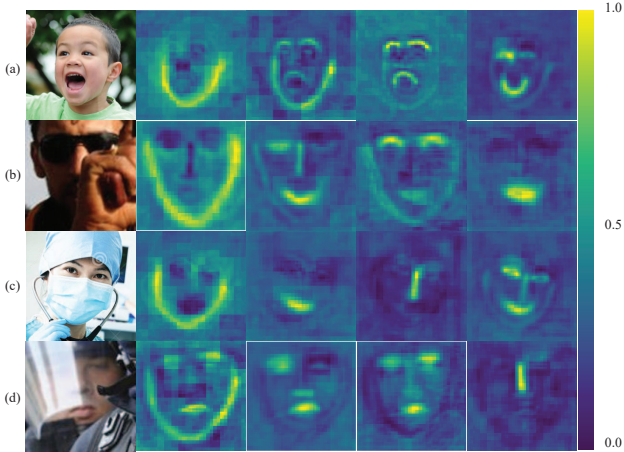


Figure 5. Boundary-aware feature maps. We visualize the 64×64 output of the last hourglass block of the SCBE module, which presents a good perception of the boundaries of cheek, nose bridge, and lips, for faces with heavy occlusions.

module in the decoding process, whose resolution are the same to the inverted order of s feature maps \mathbf{B} . We illustrate the shape constraint enhancement as:

$$\mathbf{F}_{i+1}^d = BU(\mathcal{DC}(\mathbf{F}_{s-i+1}^{e'} \otimes \mathbf{F}_i^d)) \quad (5)$$

where BU denotes the bilinear upsample, \mathcal{DC} denotes the double convolutional layers, $\mathbf{F}_{s-i+1}^{e'}$ denotes the fusion output before maxpooling layer and double convolutional layers, and \otimes denotes the channel-wise concatenation.

With multi-level boundary information, our method can obtain more uniformed landmark predictions than other methods, as shown in Fig. 6. Take the face in the third row for example, the shape of landmarks predicted by our approach is more smoother and fit better the chin than that predicted by HRNet [45] and AWing [52]. While landmark drifting and big interval (red dashed circle) occurs for HR-Net, due to the occlusion of mask, our approach is more robust against such occlusion.

4. Experiments

4.1. Dataset

We train and evaluate our method on the following popular and challenging face alignment datasets including WFLW [53], 300W [40], 300W-LP and AFLW2000-3D [66], AFLW [24], COFW [20] and COFW-68 [20].

WFLW dataset. It is a challenging 98 facial landmarks localization dataset based on the widerface dataset [59]. There are 10000 faces, we use 7500 faces for training and 2500 faces for testing. The test set is split into six subsets for evaluation which presents variations of large pose (326 images), expression (314 images), illumination(698

images), blur(773 images), make-up(206 images) and occlusion(736 images).

300W dataset. It is a widely used benchmark for evaluating facial landmarks localization algorithms. There are 3148 face images for training. The test set contains 689 faces which are split into a common subset (554 images) and a challenging subset (135 images) for validation. The test set for the competition of 300W contains 600 image samples. Each face is annotated with 68 landmarks.

300W-LP and AFLW2000-3D. 300W-LP is a synthetic dataset based on 300W dataset annotated with 68 landmarks and it contains 61225 face images with large poses ranging from 0° to 90° . AFLW2000-3D contains 2000 face images with 68 annotated landmarks. In our experiments, 300W-LP is used for training and AFLW2000-3D dataset is used for testing.

COFW and COFW-68. COFW contains 1345 images for training and 507 images for testing. Each face is annotated with 29 landmarks. COFW-68 is a reannotated dataset of COFW using the 68-landmarks annotation format of the 300W dataset.

AFLW. The widely used dataset consists of 20000 images for training. Two test sets, i.e. aflw-full(4386 images) and frontal (1314 images selected from aflw-full) are available for evaluation. Each face is annotated with 19 landmarks.

4.2. Evaluation metrics

Normalized Mean Error (NME) is a point-to-point normalized euclidian distance. NME for each image is calculated by the following formula:

$$NME(P, \hat{P}) = \frac{1}{L} \sum_{i=1}^L \frac{\|p_i - \hat{p}_i\|}{d} \quad (6)$$

where P and \hat{P} are the ground truth and predicted coordinates of landmarks. L is the number of landmarks. p_i and \hat{p}_i are the ground-truth and predicted coordinates of the i th landmark. d is the normalization factor. For the WFLW dataset, we follow [53] to use the *interocular*(outer-eye-corner distance) as the normalization factor. *Inter-pupil*(eye-center distance) is used for the COFW and 300W datasets. We use the face size $\sqrt{h_{bbox} * w_{bbox}}$ as the factor d for AFLW, AFLW2000-3D and COFW-68 dataset.

Failure Rate (FR). If an image’s NME is larger than a threshold, it is considered as a failure case. For the WFLW dataset, we follow [53] and choose 10% as the threshold. For 300W, we follow [52] and choose 8% and 10% as the thresholds, respectively.

Cumulative Error Distribution (CED). We follow [53, 52, 45] to plot the the CED curve. And Area Under Curve (AUC) is calculated based on the CED curve. Larger AUC

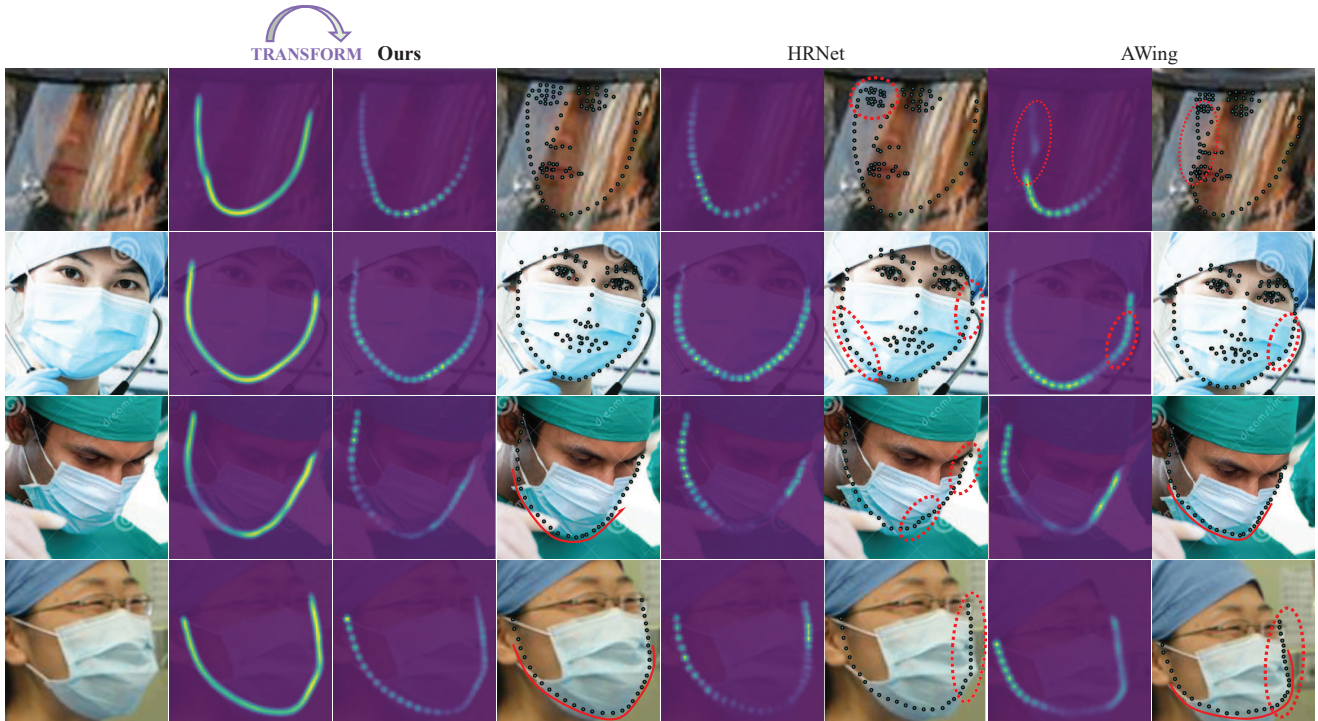


Figure 6. Examples of facial boundary adaptable landmark predictions for different methods. Compared to HRNet and AWing, our method achieved boundary-sensitive, smoother, and more uniform landmark predictions.

means that a larger portion of the test dataset is well predicted.

4.3. Implementaion details

We cropped each image by the bounding box of face provided by HRNet [45] and resized it to 256×256 as input. The SCBE module consists of 2-Stacked Hourglass Network [3] with vgg16bn stem layers(implemented by Torchvision) and the BALT module was based on UNet. Data augmentation was performed with flipping(50%), random rotation($\pm 60^\circ$), rescaling($\pm 25\%$), random coarse dropout(50%) and random brightness or darkness. During training, we chose Adam optimizer with initial learning rate 0.0001, and set the weight decay to 0. We trained the SCBE module for 140 epoch with multiplication of 0.1 at 80 and 120 epoch. Then we froze the paramters of the SCBE module to train the whole model with the same setting. We used a normal distribution with $std = 0.001$ and $mean = 0$ to initialize the parameters of stacked hourglass. The parameters of vgg16bn pre-trained on ImageNet were used to initialize stem layers. Mean quared error was adopted as the loss function to train these two modules. All experiments were conducted on PyTorch [36] with one Tesla P100 GPU(16GB). While the SCBE modules for WFLW and 300W datasets are trained using their corresponding training set, that for other datasets are directly taken from

the one trained by WFLW dataset.

4.4. WFLW dataset

The results on the WFLW dataset are shown in Table 1 and Fig 9. Compared to state-of-the-art methods such as HRNet, AWing, and LUVLi, our approach displays a significant improvement on the WFLW test set and the other six test subsets, in terms of Normalized Mean Error, Failure Rate, and Area Under the Curve. These evaluation results verify that our SCBE module and BALT module can accurately extract boundary information and efficiently transform it to landmark heatmaps. It also indicates the robustness of our method for face alignment in the wild.

4.5. 300W dataset

The results on 300W dataset and private set are shown in Table 2 and Table 3. To evaluate the capacity of our SCBE module, we also train it on the WFLW dataset and apply it to the 300W dataset for face alignment. Our method directly achieves comparative result and ranks the second-best in terms of the inter-ocular metric, which verifies the effiveness of our SCBE module and BATL module.

4.6. COFW and COFW-68 datasets

On the COFW dataset, the network is trained on the COFW training set and tested on the COFW test set. On

Table 1. Evaluation on the WFLW dataset.

Metric	Method	Testset	Pose Subset	Expression Subset	Illumination Subset	Make-up Subset	Occlusion Subset	Blur Subset
NME(%)(↓)	ESR _{CVPR 14} [5]	11.13	25.88	11.47	10.49	11.05	13.75	12.20
	SDM _{CVPR 13} [57]	10.29	24.10	11.45	9.32	9.38	13.03	11.28
	CFSS _{CVPR 15} [64]	9.07	21.36	10.09	8.30	8.74	11.76	9.96
	DVLN _{CVPR 17} [54]	6.08	11.54	6.78	5.73	5.98	7.33	6.88
	LAB _{CVPR 18} [53]	5.27	10.24	5.51	5.23	5.15	6.79	6.32
	Wing _{CVPR 18} [18]	5.11	8.75	5.36	4.93	5.41	6.37	5.81
	HRNet ₁₉ [45]	4.60	7.86	4.78	4.57	4.26	5.42	5.36
	AWing _{ICCV 19} [52]	4.36	7.38	4.58	4.32	4.27	5.19	4.96
	LUVLi _{CVPR 20} [27]	4.37	7.56	4.77	4.30	4.33	5.29	4.94
TAB(Ours)	3.94	6.70	4.11	3.84	3.85	4.56	4.45	
FR _{10%} (%)(↓)	ESR _{CVPR 14} [5]	35.24	90.18	42.04	30.80	38.84	47.28	41.40
	SDM _{CVPR 13} [57]	29.40	84.36	33.44	26.22	27.67	41.85	35.32
	CFSS _{CVPR 15} [64]	20.56	66.26	23.25	17.34	21.84	32.88	23.67
	DVLN _{CVPR 17} [54]	10.84	46.93	11.15	7.31	11.65	16.30	13.71
	LAB _{CVPR 18} [53]	7.56	28.83	6.37	6.73	7.77	13.72	10.74
	Wing _{CVPR 18} [18]	6.00	22.70	4.78	4.30	7.77	12.50	7.76
	AWing _{ICCV 19} [52]	2.84	13.50	2.23	2.58	2.91	5.98	3.75
	LUVLi _{CVPR 20} [27]	3.12	15.95	3.18	2.15	3.40	6.39	3.23
	TAB(Ours)	1.96	8.59	1.59	1.58	1.94	3.94	2.20
AUC _{10%} (↑)	ESR _{CVPR 14} [5]	0.2774	0.0177	0.1981	0.2953	0.2485	0.1946	0.2204
	SDM _{CVPR 13} [57]	0.3002	0.0226	0.2293	0.3237	0.3125	0.2060	0.2398
	CFSS _{CVPR 15} [64]	0.3659	0.0632	0.3157	0.3854	0.3691	0.2688	0.3037
	DVLN _{CVPR 17} [54]	0.4551	0.1474	0.3889	0.4743	0.4494	0.3794	0.3973
	LAB _{CVPR 18} [53]	0.5323	0.2345	0.4951	0.5433	0.5394	0.4490	0.4630
	Wing _{CVPR 18} [18]	0.5504	0.3100	0.4959	0.5408	0.5582	0.4885	0.4918
	AWing _{ICCV 19} [52]	0.5719	0.3120	0.5149	0.5777	0.5715	0.5022	0.5120
	LUVLi _{CVPR 20} [27]	0.577	0.310	0.549	0.584	0.588	0.505	0.525
	TAB(Ours)	0.6112	0.3577	0.5979	0.6203	0.6205	0.5552	0.5611

the COFW-68 dataset, the network is trained on the 300W training set and tested on the COFW-68 test set. The results on COFW and COFW-68 datasets are shown in Table 4, Table 5, and Fig 8. As shown in the results, our method outperforms all state-of-the-art methods by a significant margin. It verifies that our SCBE module and BALT module have a good generalization on faces with different number of facial landmarks.

4.7. AFLW dataset

Table 6 provides the results on AFLW dataset. Our method achieves the second-best performance among state-of-the-art methods. As only 19 landmarks are annotated for this dataset, there might be large intervals between landmarks. The large gap may interfere with the shape of facial boundary and compromise the performance of following landmark heatmap regression.

4.8. AFLW2000-3D dataset

Table 7 provides the results on AFLW2000-3D test set. For the faces with yaw angle from 0° to 60°, our method

achieves the best performance among all available models. Although the NME of our approach for faces with yaw angle from 60° to 90° is a little bit bigger than that of 2DASL [49], the mean NME of our approach still ranks the top. The results clearly suggest that our approach is robust against the large pose variations.

4.9. Ablation study

In this section, we use 300W challenging subset to validate the effectiveness of the stem layers and multi-scale features fusion, and evaluate different combinations of feature selection, i.e. single-scale (ss) and multi-scale (ms), and feature fusion, i.e. 0×, 1×, 2×, 3×.

Stem layers. Robust stem layers extract more rich and accurate local features, which boost the performance of the SCBE module. We tested different stem layers like ResNet-50 and VGG, and compared their performances in Table 8 with the baseline, which adopt the stem layers of the Hourglass networks. As shown in Table 8, the MSE, AUC, NME and FR of VGG achieved better performance than ResNet and baseline.

Table 2. Evaluation on the 300W dataset. Key=[**Best**, **Second Best**]. * indicates the SCBE module is trained on 300W dataset.

Method	Common Subset	Challenging Subset	Fullset
Inter-pupil Normalization			
CFAN _{ECCV 14} [61]	5.50	16.78	7.69
SDM _{CVPR 13} [57]	5.57	15.40	7.50
LBF _{CVPR 14} [37]	4.95	11.98	6.32
CFSS _{CVPR 15} [64]	4.73	9.98	5.76
TCDCN _{16'} [63]	4.80	8.60	5.54
MDM _{CVPR 16} [48]	4.83	10.14	5.88
RAR _{ECCV 16} [56]	4.12	8.35	4.94
DVLN _{CVPR 17} [54]	3.94	7.62	4.66
TSR _{CVPR 17} [32]	4.36	7.56	4.99
DSRN _{CVPR 18} [33]	4.12	9.68	5.21
RCN ⁺ (L+ELT) _{CVPR 18} [23]	4.20	7.78	4.90
DCFE _{ECCV 18} [50]	3.83	7.54	4.55
LAB _{CVPR 18} [53]	3.42	6.98	4.12
Wing _{CVPR 18} [18]	3.27	7.18	4.04
AWing _{ICCV 19} [52]	3.77	6.52	4.31
TAB(Ours)	3.81	6.76	4.39
Inter-ocular Normalization			
PCD-CNN _{CVPR 18} [26]	3.67	7.62	4.44
SAN _{CVPR 18} [14]	3.34	6.60	3.98
LAB _{CVPR 18} [53]	2.98	5.19	3.49
DU-Net _{ECCV 18} [47]	2.90	5.15	3.35
HRNet _{19'} [45]	2.87	5.15	3.32
AWing _{ICCV 19} [52]	2.72	4.52	3.07
LUVLi _{CVPR 20} [27]	2.76	5.16	3.23
TAB*(Ours)	2.75	4.74	3.14
TAB(Ours)	2.75	4.68	3.13

Table 3. Evaluation on 300W private dataset. Key:[**Best**, **Second Best**]

Method	NME(%) (↓)	AUC _{8%} (%) (↑)	FR _{8%} (%) (↓)
ESR _{CVPR 14} [5]	-	32.35	17.00
cGPRT _{CVPR 15} [30]	-	41.32	12.83
CFSS _{CVPR 15} [64]	-	39.81	12.30
MDM _{CVPR 16} [48]	5.05	45.32	6.80
DAN _{CVPR 17} [25]	4.30	47.00	2.67
SHN _{CVPR 17} [58]	4.05	-	-
DCFE _{ECCV 18} [50]	3.88	52.42	1.83
AWing _{ICCV 19} [52]	3.56	55.76	0.83
TAB(Ours)	3.59	55.20	0.50
	NME(%) (↓)	AUC _{10%} (%) (↑)	FR _{10%} (%) (↓)
M3-CSR _{16'} [12]	-	47.52	5.5
Fan <i>et al.</i> _{16'} [15]	-	48.02	14.83
DR + MDM _{CVPR 17} [1]	-	52.19	3.67
JMFA _{17'} [13]	-	54.85	1.00
LAB _{CVPR 18} [53]	-	58.85	0.83
AWing _{ICCV 19} [52]	3.56	64.40	0.33
TAB(Ours)	3.59	64.11	0.17

Boundary-aware features selection. Using features extracted by the SCBE module as additional information not

Table 4. Evaluation on the COFW dataset.

Method	NME	AUC _{10%} (↑)	FR _{10%} (↓)
Human [4]	5.60	-	0.00
Wu <i>et al.</i> _{ICCV 15} [55]	5.93	-	-
RAR _{ECCV 16} [56]	6.03	-	4.14
DAC-CSR _{CVPR 17} [19]	6.03	-	4.73
SHN _{CVPR 17} [58]	5.60	-	-
PCD-CNN _{CVPR 18} [26]	5.77	-	3.73
Wing _{CVPR 18} [18]	5.44	-	3.75
AWing _{ICCV 19} [52]	4.94	48.82	0.99
TAB(Ours)	4.39	56.14	0.20
	NME	AUC _{8%} (↑)	FR _{8%} (↓)
DCFE _{ECCV 18} [50]	5.27	35.86	7.29
AWing _{ICCV 19} [52]	4.94	39.11	5.52
TAB(Ours)	4.39	45.29	0.79

Table 5. Evaluation on COFW-68 dataset. [Key:*=Pretrained on 300W-LP-2D]

Method	NME(%) (↓)	AUC _{10%} (%) (↑)
SAN [*] _{CVPR 18} [14]	3.50	51.9
2D-FAN [*] _{ICCV 17} [3]	2.95	57.5
Softlabel [*] _{ICCV 19} [7]	2.92	57.9
KDN [*] _{ICCV 19} [7]	2.73	60.1
LUVLi [*] _{CVPR 20} [27]	2.57	63.4
TAB(Ours)	2.43	65.4

Table 6. Evaluation on AFLW dataset.

Method	Full(%) (↓)	Frontal(%) (↓)
CFSS _{CVPR 15} [64]	3.92	2.68
CCL _{CVPR 16} [65]	2.72	2.17
TSR _{CVPR 17} [32]	2.17	-
DAC-OSR _{CVPR 17} [19]	2.27	1.81
LLL _{ICCV 19} [38]	1.97	-
SAN _{CVPR 18} [14]	1.91	1.85
DSRN _{CVPR 18} [33]	1.86	-
LAB _{CVPR 18} [53]	1.85	1.62
HRNet _{19'} [45]	1.57	1.46
LUVLi _{CVPR 20} [27]	1.39	1.19
TAB(Ours)	1.47	1.25

only accelerates the convergence of the BALT module, but also enhances the shape constraint of facial boundary on landmarks. How to choose these features? We have tried single-scale feature (ss) and multi-scale features (ms) selected from the last hourglass network. While single-scale feature only uses the output of the last convolutional layers before heatmap predictions, multi-scale features fuse the s different output of the last hourglass network. We report the AUC, NME, and FR of these selections in Table 9. It can be observed that multi-scale features are better than single-



Figure 7. Example results on WFLW six test subsets and AFLW dataset, which justify the robustness of our method to faces with blur, expression, make-up, heavy occlusion, illumination, and large poses.

Table 7. Evaluation on AFLW2000-3D dataset(68 2D landmarks). The NME for faces with different yaw angles are reported.

Methods	NME(%)(\downarrow)			
	0° to 30°	30° to 60°	60° to 90°	Mean
SDM _{CVPR 13} [57]	3.67	4.94	9.67	6.12
3DDFA _{CVPR 16} [66]	3.78	4.54	7.93	5.42
3DDFA + SDM _{CVPR 16} [66]	3.43	4.24	7.17	5.42
Yu <i>et al.</i> _{ICCV 17} [60]	3.62	6.06	9.56	-
3DSTN _{ICCV 17} [2]	3.15	4.33	5.98	4.49
DeFA _{ICCV 17} [31]	-	-	-	4.50
PRNnet _{ECCV 18} [17]	2.75	3.51	4.61	3.62
2DASL _{TMM 20} [49]	2.75	3.44	4.41	3.53
TAB(Ours)	2.44	3.23	4.60	3.42

Table 8. Evaluation on 300W challenging subset with different stem layers. MSE indicates the mean squared error between ground-truth and predicted boundary heatmaps.

Stem	MSE	AUC _{10%} (%)(\uparrow)	NME(%)(\downarrow)	FR _{8%} (%)(\downarrow)
baseline	0.002536	51.54	4.86	2.96
resnet	0.002503	52.36	4.77	2.22
vgg	0.002442	52.98	4.70	2.22

Table 9. Evaluation on 300W challenging subset with different feature selections.

Feature	AUC _{10%} (%)(\uparrow)	NME(%)(\downarrow)	FR _{8%} (%)(\downarrow)
ss	52.24	4.78	2.22
ms	52.98	4.70	2.22



Figure 8. Example results on AFLW2000, 300W, COFW, and COFW-68 datasets.

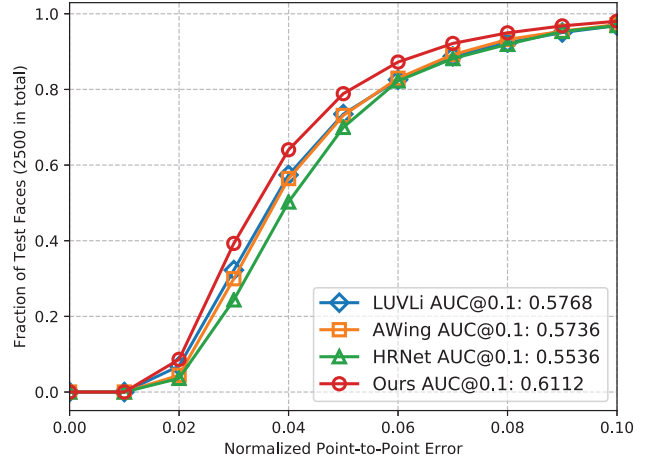


Figure 9. CED for WFLW testset (98 landmarks). AUC@0.1 is also reported.

Table 10. Evaluation on 300W challenging subset with different feature fusion settings.

Fusion	AUC _{10%} (%)(\uparrow)	NME(%)(\downarrow)	FR _{8%} (%)(\downarrow)
0 \times	51.35	4.87	3.70
1 \times	52.56	4.74	2.22
2 \times	52.98	4.70	2.22
3 \times	52.68	4.73	2.22

scale feature.

Features fusion. We tried 0 \times , 1 \times , 2 \times , and 3 \times features fusion settings in the BALT module (note that, 0 \times means no features fusion in the encoding process). We report the AUC, NME, and FR of these settings in Table 10. It can be observed that the model with features fusion 1 \times , 2 \times , and 3 \times generally achieves better performance than that without feature fusion (0 \times). While same FR was

achieved for different fusion settings, $2\times$ strategy achieved the best AUC and NME.

5. Discussion and Conclusion

In this paper, we present a two-stage but end-to-end method to deal with issues of occlusion, large pose, and expression, etc., in face alignment task. By leveraging the geometric structure of faces and the spatial information of heatmaps, our method can easily learn a shape constrained transformation to get boundary-aware landmark heatmap predictions. Experiment results on widely used datasets verify the effectiveness and great potential of our approach. When GeForce GTX TITAN X GPU(12GB) is concerned, the size and processing speed of our model with 2-stacked hourglass are 86.9MB and 27ms, respectively; the size and processing speed for 1-stacked hourglass are 64.5MB and 17ms, respectively.

We believe the unique facial structure is the key to localize facial landmarks [53], due to the fact that (1) The number of annotated facial landmarks is increasing and getting denser, which fits the shape of face better. (2) The facial structure information is more likely to be reserved and estimated on unconstrained scenes. Considerable attention could be paid to the analysis between facial structure and facial landmarks for further improvements in face alignment task.

References

- [1] Riza Alp Guler, George Trigeorgis, Epameinondas Antonakos, Patrick Snape, Stefanos Zafeiriou, and Iasonas Kokkinos. Densereg: Fully convolutional dense shape regression in-the-wild. In *Proceedings of the IEEE Conference on Computer Vision and Pattern Recognition*, pages 6799–6808, 2017. 8
- [2] Chandrasekhar Bhagavatula, Chenchen Zhu, Khoa Luu, and Marios Savvides. Faster than real-time facial alignment: A 3d spatial transformer network approach in unconstrained poses. In *Proceedings of the IEEE International Conference on Computer Vision*, pages 3980–3989, 2017. 9
- [3] Adrian Bulat and Georgios Tzimiropoulos. How far are we from solving the 2d & 3d face alignment problem? (and a dataset of 230,000 3d facial landmarks). In *International Conference on Computer Vision*, 2017. 3, 6, 8
- [4] Xavier P Burgos-Artizzu, Pietro Perona, and Piotr Dollár. Robust face landmark estimation under occlusion. In *Proceedings of the IEEE international conference on computer vision*, pages 1513–1520, 2013. 8
- [5] Xudong Cao, Yichen Wei, Fang Wen, and Jian Sun. Face alignment by explicit shape regression. *International Journal of Computer Vision*, 107(2):177–190, 2014. 7, 8
- [6] Zhe Cao, Gines Hidalgo, Tomas Simon, Shih-En Wei, and Yaser Sheikh. Openpose: realtime multi-person 2d pose estimation using part affinity fields. *arXiv preprint arXiv:1812.08008*, 2018. 3
- [7] Lisha Chen, Hui Su, and Qiang Ji. Face alignment with kernel density deep neural network. In *Proceedings of the IEEE International Conference on Computer Vision*, pages 6992–7002, 2019. 8
- [8] Timothy F. Cootes, Gareth J. Edwards, and Christopher J. Taylor. Active appearance models. *IEEE Transactions on pattern analysis and machine intelligence*, 23(6):681–685, 2001. 2
- [9] Arnaud Dapogny, Kevin Bailly, and Matthieu Cord. Decafa: Deep convolutional cascade for face alignment in the wild. In *Proceedings of the IEEE International Conference on Computer Vision*, pages 6893–6901, 2019. 3
- [10] Jia Deng, Wei Dong, Richard Socher, Li-Jia Li, Kai Li, and Li Fei-Fei. Imagenet: A large-scale hierarchical image database. In *2009 IEEE conference on computer vision and pattern recognition*, pages 248–255. Ieee, 2009. 2
- [11] Jiankang Deng, Jia Guo, Niannan Xue, and Stefanos Zafeiriou. Arcface: Additive angular margin loss for deep face recognition. In *The IEEE Conference on Computer Vision and Pattern Recognition (CVPR)*, June 2019. 1
- [12] Jiankang Deng, Qingshan Liu, Jing Yang, and Dacheng Tao. M3 csr: Multi-view, multi-scale and multi-component cascade shape regression. *Image and Vision Computing*, 47:19–26, 2016. 8
- [13] Jiankang Deng, George Trigeorgis, Yuxiang Zhou, and Stefanos Zafeiriou. Joint multi-view face alignment in the wild. *IEEE Transactions on Image Processing*, 28(7):3636–3648, 2019. 8
- [14] Xuanyi Dong, Yan Yan, Wanli Ouyang, and Yi Yang. Style aggregated network for facial landmark detection. In *Proceedings of the IEEE Conference on Computer Vision and Pattern Recognition*, pages 379–388, 2018. 8
- [15] Haoqiang Fan and Erjin Zhou. Approaching human level facial landmark localization by deep learning. *Image and Vision Computing*, 47:27–35, 2016. 8
- [16] Hao-Shu Fang, Shuqin Xie, Yu-Wing Tai, and Cewu Lu. Rmpe: Regional multi-person pose estimation. In *Proceedings of the IEEE International Conference on Computer Vision*, pages 2334–2343, 2017. 3
- [17] Yao Feng, Fan Wu, Xiaohu Shao, Yanfeng Wang, and Xi Zhou. Joint 3d face reconstruction and dense alignment with position map regression network. In *Proceedings of the European Conference on Computer Vision (ECCV)*, pages 534–551, 2018. 1, 9
- [18] Zhen-Hua Feng, Josef Kittler, Muhammad Awais, Patrik Huber, and Xiao-Jun Wu. Wing loss for robust facial landmark localisation with convolutional neural networks. In *Computer Vision and Pattern Recognition (CVPR), 2018 IEEE Conference on*, pages 2235–2245. IEEE, 2018. 3, 7, 8
- [19] Zhen-Hua Feng, Josef Kittler, William Christmas, Patrik Huber, and Xiao-Jun Wu. Dynamic attention-controlled cascaded shape regression exploiting training data augmentation and fuzzy-set sample weighting. In *Proceedings of the IEEE Conference on Computer Vision and Pattern Recognition*, pages 2481–2490, 2017. 8
- [20] Golnaz Ghiasi and Charless C Fowlkes. Occlusion coherence: Detecting and localizing occluded faces. *arXiv preprint arXiv:1506.08347*, 2015. 5

- [21] Xiaojie Guo, Siyuan Li, Jinke Yu, Jiawan Zhang, Jiayi Ma, Lin Ma, Wei Liu, and Haibin Ling. Pffd: a practical facial landmark detector. *arXiv preprint arXiv:1902.10859*, 2019. 3
- [22] Kaiming He, Xiangyu Zhang, Shaoqing Ren, and Jian Sun. Deep residual learning for image recognition. In *Proceedings of the IEEE conference on computer vision and pattern recognition*, pages 770–778, 2016. 2
- [23] Sina Honari, Pavlo Molchanov, Stephen Tyree, Pascal Vincent, Christopher Pal, and Jan Kautz. Improving landmark localization with semi-supervised learning. In *Proceedings of the IEEE Conference on Computer Vision and Pattern Recognition*, pages 1546–1555, 2018. 8
- [24] Martin Koestinger, Paul Wohlhart, Peter M Roth, and Horst Bischof. Annotated facial landmarks in the wild: A large-scale, real-world database for facial landmark localization. In *2011 IEEE international conference on computer vision workshops (ICCV workshops)*, pages 2144–2151. IEEE, 2011. 5
- [25] Marek Kowalski, Jacek Naruniec, and Tomasz Trzcinski. Deep alignment network: A convolutional neural network for robust face alignment. In *Proceedings of the IEEE Conference on Computer Vision and Pattern Recognition Workshops*, pages 88–97, 2017. 3, 8
- [26] Amit Kumar and Rama Chellappa. Disentangling 3d pose in a dendritic cnn for unconstrained 2d face alignment. In *Proceedings of the IEEE Conference on Computer Vision and Pattern Recognition*, pages 430–439, 2018. 8
- [27] Abhinav Kumar, Tim K Marks, Wenxuan Mou, Ye Wang, Michael Jones, Anoop Cherian, Toshiaki Koike-Akino, Xiaoming Liu, and Chen Feng. Luvli face alignment: Estimating landmarks’ location, uncertainty, and visibility likelihood. *arXiv preprint arXiv:2004.02980*, 2020. 7, 8
- [28] Hei Law and Jia Deng. Cornernet: Detecting objects as paired keypoints. In *Proceedings of the European Conference on Computer Vision (ECCV)*, pages 734–750, 2018. 3
- [29] Yann LeCun, Léon Bottou, Yoshua Bengio, and Patrick Haffner. Gradient-based learning applied to document recognition. *Proceedings of the IEEE*, 86(11):2278–2324, 1998. 2
- [30] Donghoon Lee, Hyunsin Park, and Chang D Yoo. Face alignment using cascade gaussian process regression trees. In *Proceedings of the IEEE Conference on Computer Vision and Pattern Recognition*, pages 4204–4212, 2015. 8
- [31] Yaojie Liu, Amin Jourabloo, William Ren, and Xiaoming Liu. Dense face alignment. In *Proceedings of the IEEE International Conference on Computer Vision Workshops*, pages 1619–1628, 2017. 9
- [32] Jiangjing Lv, Xiaohu Shao, Junliang Xing, Cheng Cheng, and Xi Zhou. A deep regression architecture with two-stage re-initialization for high performance facial landmark detection. In *Proceedings of the IEEE conference on computer vision and pattern recognition*, pages 3317–3326, 2017. 8
- [33] Xin Miao, Xiantong Zhen, Xianglong Liu, Cheng Deng, Vasilis Athitsos, and Heng Huang. Direct shape regression networks for end-to-end face alignment. In *Proceedings of the IEEE Conference on Computer Vision and Pattern Recognition*, pages 5040–5049, 2018. 8
- [34] Stephen Milborrow and Fred Nicolls. Locating facial features with an extended active shape model. In *European conference on computer vision*, pages 504–513. Springer, 2008. 2
- [35] Alejandro Newell, Kaiyu Yang, and Jia Deng. Stacked hourglass networks for human pose estimation. In *European conference on computer vision*, pages 483–499. Springer, 2016. 2
- [36] Adam Paszke, Sam Gross, Francisco Massa, Adam Lerer, James Bradbury, Gregory Chanan, Trevor Killeen, Zeming Lin, Natalia Gimelshein, Luca Antiga, et al. Pytorch: An imperative style, high-performance deep learning library. In *Advances in Neural Information Processing Systems*, pages 8024–8035, 2019. 6
- [37] Shaoqing Ren, Xudong Cao, Yichen Wei, and Jian Sun. Face alignment at 3000 fps via regressing local binary features. In *Proceedings of the IEEE Conference on Computer Vision and Pattern Recognition*, pages 1685–1692, 2014. 8
- [38] Joseph P Robinson, Yuncheng Li, Ning Zhang, Yun Fu, and Sergey Tulyakov. Laplace landmark localization. In *Proceedings of the IEEE International Conference on Computer Vision*, pages 10103–10112, 2019. 8
- [39] Olaf Ronneberger, Philipp Fischer, and Thomas Brox. U-net: Convolutional networks for biomedical image segmentation. In *International Conference on Medical image computing and computer-assisted intervention*, pages 234–241. Springer, 2015. 2
- [40] Christos Sagonas, Georgios Tzimiropoulos, Stefanos Zafeiriou, and Maja Pantic. 300 faces in-the-wild challenge: The first facial landmark localization challenge. In *Proceedings of the IEEE International Conference on Computer Vision Workshops*, pages 397–403, 2013. 5
- [41] Jason Saragih and Roland Goecke. A nonlinear discriminative approach to aam fitting. In *2007 IEEE 11th International Conference on Computer Vision*, pages 1–8. IEEE, 2007. 2
- [42] Florian Schroff, Dmitry Kalenichenko, and James Philbin. Facenet: A unified embedding for face recognition and clustering. In *The IEEE Conference on Computer Vision and Pattern Recognition (CVPR)*, June 2015. 1
- [43] Karen Simonyan and Andrew Zisserman. Very deep convolutional networks for large-scale image recognition. *arXiv preprint arXiv:1409.1556*, 2014. 2
- [44] Ke Sun, Bin Xiao, Dong Liu, and Jingdong Wang. Deep high-resolution representation learning for human pose estimation. In *CVPR*, 2019. 3
- [45] Ke Sun, Yang Zhao, Borui Jiang, Tianheng Cheng, Bin Xiao, Dong Liu, Yadong Mu, Xinggang Wang, Wenyu Liu, and Jingdong Wang. High-resolution representations for labeling pixels and regions. *arXiv preprint arXiv:1904.04514*, 2019. 5, 6, 7, 8
- [46] Yi Sun, Xiaogang Wang, and Xiaoou Tang. Deep convolutional network cascade for facial point detection. In *Proceedings of the IEEE conference on computer vision and pattern recognition*, pages 3476–3483, 2013. 2
- [47] Zhiqiang Tang, Xi Peng, Shijie Geng, Lingfei Wu, Shaoting Zhang, and Dimitris Metaxas. Quantized densely connected u-nets for efficient landmark localization. In *Proceedings*

- of the *European Conference on Computer Vision (ECCV)*, pages 339–354, 2018. 8
- [48] George Trigeorgis, Patrick Snape, Mihalis A Nicolaou, Epameinondas Antonakos, and Stefanos Zafeiriou. Mnemonic descent method: A recurrent process applied for end-to-end face alignment. In *Proceedings of the IEEE Conference on Computer Vision and Pattern Recognition*, pages 4177–4187, 2016. 8
- [49] Xiaoguang Tu, Jian Zhao, Mei Xie, Zihang Jiang, Akshaya Balamurugan, Yao Luo, Yang Zhao, Lingxiao He, Zheng Ma, and Jiashi Feng. 3d face reconstruction from a single image assisted by 2d face images in the wild. *IEEE Transactions on Multimedia*, PP:1–1, 05 2020. 1, 7, 9
- [50] Roberto Valle, Jose M Buenaposada, Antonio Valdes, and Luis Baumela. A deeply-initialized coarse-to-fine ensemble of regression trees for face alignment. In *Proceedings of the European Conference on Computer Vision (ECCV)*, pages 585–601, 2018. 8
- [51] Jun Wan, Jing Li, Zhihui Lai, Bo Du, and Lefei Zhang. Robust face alignment by cascaded regression and de-occlusion. *Neural Networks*, 123:261–272, 2020. 3
- [52] Xinyao Wang, Liefeng Bo, and Li Fuxin. Adaptive wing loss for robust face alignment via heatmap regression. In *Proceedings of the IEEE International Conference on Computer Vision*, pages 6971–6981, 2019. 3, 5, 7, 8
- [53] Wayne Wu, Chen Qian, Shuo Yang, Quan Wang, Yici Cai, and Qiang Zhou. Look at boundary: A boundary-aware face alignment algorithm. In *CVPR*, 2018. 1, 3, 5, 7, 8, 10
- [54] Wenyang Wu and Shuo Yang. Leveraging intra and inter-dataset variations for robust face alignment. In *Proceedings of the IEEE conference on computer vision and pattern recognition workshops*, pages 150–159, 2017. 7, 8
- [55] Yue Wu and Qiang Ji. Robust facial landmark detection under significant head poses and occlusion. In *Proceedings of the IEEE International Conference on Computer Vision*, pages 3658–3666, 2015. 8
- [56] Shengtao Xiao, Jiashi Feng, Junliang Xing, Hanjiang Lai, Shuicheng Yan, and Ashraf Kassim. Robust facial landmark detection via recurrent attentive-refinement networks. In *European conference on computer vision*, pages 57–72. Springer, 2016. 8
- [57] Xuehan Xiong and Fernando De la Torre. Supervised descent method and its applications to face alignment. In *Proceedings of the IEEE conference on computer vision and pattern recognition*, pages 532–539, 2013. 7, 8, 9
- [58] Jing Yang, Qingshan Liu, and Kaihua Zhang. Stacked hourglass network for robust facial landmark localisation. In *Proceedings of the IEEE Conference on Computer Vision and Pattern Recognition Workshops*, pages 79–87, 2017. 8
- [59] Shuo Yang, Ping Luo, Chen Change Loy, and Xiaoou Tang. Wider face: A face detection benchmark. In *IEEE Conference on Computer Vision and Pattern Recognition (CVPR)*, 2016. 5
- [60] Ronald Yu, Shunsuke Saito, Haoxiang Li, Duygu Ceylan, and Hao Li. Learning dense facial correspondences in unconstrained images. In *Proceedings of the IEEE International Conference on Computer Vision*, pages 4723–4732, 2017. 9
- [61] Jie Zhang, Shiguang Shan, Meina Kan, and Xilin Chen. Coarse-to-fine auto-encoder networks (cfan) for real-time face alignment. In *European conference on computer vision*, pages 1–16. Springer, 2014. 8
- [62] K. Zhang, Z. Zhang, Z. Li, and Y. Qiao. Joint face detection and alignment using multitask cascaded convolutional networks. *IEEE Signal Processing Letters*, 23(10):1499–1503, Oct 2016. 3
- [63] Zhanpeng Zhang, Ping Luo, Chen Change Loy, and Xiaoou Tang. Learning deep representation for face alignment with auxiliary attributes. *IEEE transactions on pattern analysis and machine intelligence*, 38(5):918–930, 2015. 8
- [64] Shizhan Zhu, Cheng Li, Chen Change Loy, and Xiaoou Tang. Face alignment by coarse-to-fine shape searching. In *Proceedings of the IEEE conference on computer vision and pattern recognition*, pages 4998–5006, 2015. 7, 8
- [65] Shizhan Zhu, Cheng Li, Chen-Change Loy, and Xiaoou Tang. Unconstrained face alignment via cascaded compositional learning. In *Proceedings of the IEEE Conference on Computer Vision and Pattern Recognition*, pages 3409–3417, 2016. 8
- [66] Xiangyu Zhu, Zhen Lei, Xiaoming Liu, Hailin Shi, and Stan Z Li. Face alignment across large poses: A 3d solution. In *Proceedings of the IEEE conference on computer vision and pattern recognition*, pages 146–155, 2016. 5, 9